

Compositional and Fabrication Cycle Optimization of Ceria-Zirconia-Supported Mo-Based Catalysts for NH<sub>3</sub>-SCR NO<sub>x</sub> Reduction

*Original*

Compositional and Fabrication Cycle Optimization of Ceria-Zirconia-Supported Mo-Based Catalysts for NH<sub>3</sub>-SCR NO<sub>x</sub> Reduction / Spiridigliozzi, Luca; Monfreda, Viviana; Esposito, Serena; Tammaro, Olimpia; Blangetti, Nicola; Deorsola, Fabio Alessandro; Dell'Agli, Gianfranco. - In: INORGANICS. - ISSN 2304-6740. - 12:8(2024).  
[10.3390/inorganics12080217]

*Availability:*

This version is available at: 11583/2995884 since: 2024-12-23T15:37:25Z

*Publisher:*

Multidisciplinary Digital Publishing Institute (MDPI)

*Published*

DOI:10.3390/inorganics12080217

*Terms of use:*

This article is made available under terms and conditions as specified in the corresponding bibliographic description in the repository

*Publisher copyright*

(Article begins on next page)

## Article

# Compositional and Fabrication Cycle Optimization of Ceria-Zirconia-Supported Mo-Based Catalysts for NH<sub>3</sub>-SCR NO<sub>x</sub> Reduction

Luca Spiridigliozzi <sup>1,\*</sup>, Viviana Monfreda <sup>1</sup>, Serena Esposito <sup>2</sup>, Olimpia Tammaro <sup>2</sup>, Nicola Blangetti <sup>2</sup>, Fabio Alessandro Deorsola <sup>2</sup> and Gianfranco Dell'Agli <sup>1,\*</sup>

<sup>1</sup> Dipartimento di Ingegneria Civile e Meccanica, Università degli Studi di Cassino e del Lazio Meridionale, Via G. Di Biasio, 43, I-03043 Cassino, FR, Italy; viviana.monfreda@unicas.it

<sup>2</sup> Dipartimento di Scienza Applicata e Tecnologia e Unità INSTM Torino-Politecnico, Corso Duca degli Abruzzi, 24, I-10129 Torino, Italy; serena\_esposito@polito.it (S.E.); olimpia.tammaro@polito.it (O.T.); nicola.blangetti@polito.it (N.B.); fabio.deorsola@polito.it (F.A.D.)

\* Correspondence: l.spiridigliozzi@unicas.it (L.S.); gianfranco.dellagli@unicas.it (G.D.)

**Abstract:** The reduction of nitrogen oxides (NO<sub>x</sub>), critical pollutants from stationary to mobile sources, mainly relies on the selective catalytic reduction (NH<sub>3</sub>-SCR) method, employing ammonia to reduce NO<sub>x</sub> into nitrogen and water. However, conventional catalysts, while effective, pose both environmental and operational challenges. This study investigates ceria-zirconia-supported molybdenum-based catalysts, exploring the effects of zirconium doping and different catalyst synthesis techniques, i.e., co-precipitation and impregnation. The catalytic performance of the differently prepared samples was significantly influenced by the molybdenum incorporation method and the zirconium content within the ceria-zirconia support. Co-precipitation at higher temperatures resulted in catalysts with better structural attributes but slightly lower catalytic activity compared to those prepared via impregnation. Optimal NO<sub>x</sub> reduction (close to 100%) was observed at a 15 mol% zirconium doping level when using the impregnation method.

**Keywords:** NH<sub>3</sub>-SCR; NO<sub>x</sub> reduction; Ce-Zr-Mo catalysts; molybdenum oxide



**Citation:** Spiridigliozzi, L.; Monfreda, V.; Esposito, S.; Tammaro, O.; Blangetti, N.; Deorsola, F.A.; Dell'Agli, G. Compositional and Fabrication Cycle Optimization of Ceria-Zirconia-Supported Mo-Based Catalysts for NH<sub>3</sub>-SCR NO<sub>x</sub> Reduction. *Inorganics* **2024**, *12*, 217. <https://doi.org/10.3390/inorganics12080217>

Academic Editors: Eleonora Aneggi, Geun-Ho Han and Tobias Krämer

Received: 11 July 2024

Revised: 2 August 2024

Accepted: 8 August 2024

Published: 10 August 2024



**Copyright:** © 2024 by the authors. Licensee MDPI, Basel, Switzerland. This article is an open access article distributed under the terms and conditions of the Creative Commons Attribution (CC BY) license (<https://creativecommons.org/licenses/by/4.0/>).

## 1. Introduction

The pressing environmental and health challenges posed by nitrogen oxide (NO<sub>x</sub>) emissions, derived from both stationary sources such as power plants and steel plants [1,2] and mobile sources such as automobiles and heavy-duty vehicles [3,4], underscore the critical need for effective emission control technologies. Among these, selective catalytic reduction (NH<sub>3</sub>-SCR) has emerged as a principal technology for controlling NO<sub>x</sub> emissions [5–7]. NH<sub>3</sub>-SCR leverages ammonia (NH<sub>3</sub>) as a reducing agent to convert NO<sub>x</sub> into gaseous nitrogen (N<sub>2</sub>) and water (H<sub>2</sub>O) within a specific temperature range [5], thus representing a widely adopted denitrification technology.

Catalysts play a pivotal role in the NH<sub>3</sub>-SCR process, with their performance and stability being crucial for the technology's large-scale industrial application [7]. Historically, the V<sub>2</sub>O<sub>5</sub> catalyst (differently supported) has been dominant in the industry due to its high catalytic efficiency [8–13]. However, V<sub>2</sub>O<sub>5</sub>'s biological toxicity [14] and relatively poor thermal stability [15] have limited its broader application. Moreover, issues such as difficult recyclability and the potential for secondary pollution pose additional environmental and safety concerns [16,17].

In the quest for more efficient NH<sub>3</sub>-SCR catalysts, transition metal oxides such as Mn, Cu, and Fe have demonstrated higher activity at lower temperatures [18–22]. Nonetheless, their susceptibility to sulfur poisoning remains a significant barrier to industrial use [23,24].

Despite meaningful progress achieved through elemental doping, novel preparation methods, and carrier loading, these strategies alone have proven insufficient to overcome the inherent limitations of current catalyst formulations [25,26].

This synthesis of current research highlights a concerted effort to develop low-temperature  $\text{NH}_3$ -SCR catalysts with enhanced chemical resistance to  $\text{H}_2\text{O}$  and  $\text{SO}_2$ . Specifically, the research efforts should be directed to develop catalyst structures that not only mitigate  $\text{NO}_x$  emissions efficiently but also address the operational and environmental drawbacks of the existing solutions. Molybdenum (Mo), as an active catalyst component, has recently gained attention in the context of  $\text{NO}_x$  reduction, especially within the context of selective catalytic reduction (SCR) processes [27–29]. The use of molybdenum, often in conjunction with other metals such as vanadium (V) and tungsten (W), is primarily due to its beneficial properties that enhance catalytic performance for  $\text{NO}_x$  reduction [30,31]. Molybdenum, when integrated into the catalyst structure, can help in expanding the operating temperature range, thereby making the catalyst more versatile for different industrial applications that operate at varying temperatures [32]. The commonly accepted mechanism for the  $\text{NO}_x$  reduction over Mo is the bifunctional mechanism whereby the  $\text{NH}_3$  is activated on the acidic sites of  $\text{MoO}_3$  (or  $\text{WO}_3$ ) while the Ce component, through the  $\text{Ce}^{4+}/3^+$  pair, is able to reduce the  $\text{NO}_x$  [33,34].

Moreover, Mo modifies the surface properties of the catalyst, contributing to improving the electron transfer processes within the catalyst and thus facilitating the reduction of  $\text{NO}_x$  to  $\text{N}_2$  and  $\text{H}_2\text{O}$  more efficiently. This is particularly important for low-temperature applications where achieving sufficient catalytic activity can be challenging. Finally, molybdenum has been shown to improve the resistance of catalysts to sulfur poisoning, maintaining catalytic activity and longevity in environments with high  $\text{SO}_2$  concentrations [35].

However, the challenge of anchoring highly reactive Mo species onto an appropriate support still poses practical issues [36,37], as well as the balance between the acid/redox sites and surface exposure/availability must be optimized for the best catalyst performance for such systems.

Therefore, this study seeks to evaluate differently Zr-doped ceria ( $\text{CeO}_2$ ) as a support for active and durable Mo-based catalysts. Although Zr-doped ceria has been widely recognized for its exceptional qualities as a heterogeneous catalyst over recent years [38–42], its application in dispersing active Mo-based catalysts specifically for  $\text{NO}_x$  reduction reactions remains partially unexplored, to the best of our knowledge. In this context, we have used a simple and cheap co-precipitation technique for synthesizing both undoped and Zr-doped ceria supports, subsequently subjected to wet impregnation with the Mo-based active catalysts (with MoO as 10 wt% of the support). The impact of the precipitating temperature (and the related MoO addition mode) on the dispersion and effectiveness of the catalyst has been studied, highlighting the structural and surface characteristics of the samples. Finally, the variously prepared samples have been tested in terms of their catalytic SCR activity.

## 2. Results and Discussion

All the catalyst samples prepared contain a nominal molybdenum oxide content of 10 wt%, and their different labels are reported in Table 1, also containing a summary of the conditions under which the synthesis was carried out.

Figure 1 shows the diffraction patterns of all the impregnated catalysts (i.e.,  $\text{CeZr}_0\text{Mo}_{10}\text{-imp}$ ,  $\text{CeZr}_{15}\text{Mo}_{10}\text{-imp}$ , and  $\text{CeZr}_{30}\text{Mo}_{10}\text{-imp}$ ).

First, a clear trend in terms of “degree of crystallization” is observable in Figure 1: from sample  $\text{CeZr}_0\text{Mo}_{10}\text{-imp}$  (Zr = 0%), the better-crystallized one, to sample  $\text{CeZr}_{30}\text{Mo}_{10}\text{-imp}$  (Zr = 30%), the worst-crystallized one (and likely also characterized by the presence of some amorphous phase). Such a remarkable difference in crystallinity, in terms of both the amount of crystallized material and crystallite size, is clearly highlighted in Figure 1 by the reflections at high  $2\theta$  angles, i.e., corresponding to planes (331) and (420), which are well resolved for the sample  $\text{CeZr}_0\text{Mo}_{10}\text{-imp}$  (with relatively larger crystallites), whereas for

sample CeZr<sub>30</sub>Mo<sub>10</sub>\_imp, those reflections are barely perceivable, suggesting very small crystallites. The diffraction pattern of sample CeZr<sub>15</sub>Mo<sub>10</sub>\_imp is intermediate to the previous ones. Such a trend is very likely due to the different amounts of ZrO<sub>2</sub> doping within the samples. Indeed, pure, as-precipitated ceria derived by addition of ammonia to cerium (III) nitrate solution is very prone to crystallization in fluorite structure, so that a mild thermal treatment (i.e., at about 300 °C) suffices to obtain a well-crystallized system [43,44]. Conversely, a full crystallization of zirconia precipitated through ammonia requires higher temperatures, i.e., around 440 °C, and leads to the formation of tetragonal zirconia [45]. Therefore, in the sample without zirconium (pure ceria support), the calcination treatment used in the present work (i.e., 450 °C for 1 h) led to full crystallization, whereas the fluorite-structured samples CeZr<sub>15</sub>Mo<sub>10</sub>\_imp and CeZr<sub>30</sub>Mo<sub>10</sub>\_imp are only partially crystallized due to the zirconium doping.

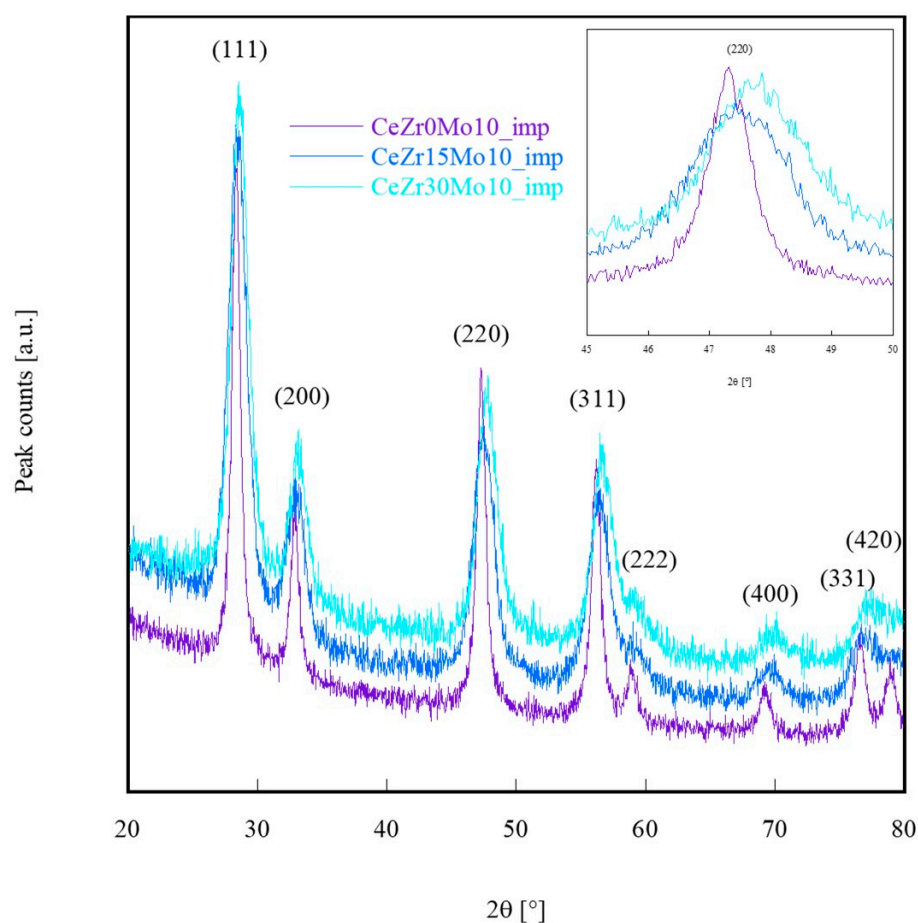


**Figure 1.** XRD patterns of samples CeZr<sub>0</sub>Mo<sub>10</sub>\_imp, CeZr<sub>15</sub>Mo<sub>10</sub>\_imp, and CeZr<sub>30</sub>Mo<sub>10</sub>\_imp, calcined at 450 °C for 1h. The inset highlights the detail of the (220) peak of CeZr<sub>0</sub>Mo<sub>10</sub>\_imp, CeZr<sub>15</sub>Mo<sub>10</sub>\_imp, and CeZr<sub>30</sub>Mo<sub>10</sub>\_imp diffraction patterns.

Additionally, upon careful examination of Figure 1, one can observe an increasing positive shift of the Bragg angles (see inset in Figure 1, where the enlargement of the peak corresponding to the crystallographic plane with Miller index (220) of fluorite with increasing zirconium content is shown). Such observed shift is related to the decrease in the lattice parameter of fluorite from sample CeZr<sub>0</sub>Mo<sub>10</sub>\_imp to sample CeZr<sub>30</sub>Mo<sub>10</sub>\_imp, indicative of the effect of partial substitution of the Ce<sup>4+</sup> ion (cationic radius 0.97 Å in coordination VIII [46]) with the Zr<sup>4+</sup> ion (cationic radius 0.84 Å in coordination VIII [46]) in the ceria lattice (see also Table 2). Essentially, the absence of Mo-containing salts during the co-precipitation step with NH<sub>3</sub> leads to the formation of a Ce-Zr substitutional solid

solution, consequently causing a decrease in the lattice parameter with increasing Zr content. Conversely, the addition of Mo in the subsequent impregnation step is not detectable via XRD, very likely being present in an amorphous form.

**Table 1.** Prepared catalysts and their labeling.

Sample Labeling	Composition	Mo Addition	Precipitation Temperature
CeZr <sub>0</sub> Mo <sub>10</sub> _imp	10MoO <sub>3</sub> /CeO <sub>2</sub>	Impregnation	r.t.
CeZr <sub>15</sub> Mo <sub>10</sub> _imp	10MoO <sub>3</sub> /Ce <sub>0.85</sub> Zr <sub>0.15</sub> O <sub>2</sub>	Impregnation	r.t.
CeZr <sub>30</sub> Mo <sub>10</sub> _imp	10MoO <sub>3</sub> /Ce <sub>0.70</sub> Zr <sub>0.30</sub> O <sub>2</sub>	Impregnation	r.t.
CeZr <sub>0</sub> Mo <sub>10</sub> _copr	10MoO <sub>3</sub> /CeO <sub>2</sub>	Co-precipitation	90 °C
CeZr <sub>15</sub> Mo <sub>10</sub> _copr	10MoO <sub>3</sub> /Ce <sub>0.85</sub> Zr <sub>0.15</sub> O <sub>2</sub>	Co-precipitation	90 °C
CeZr <sub>30</sub> Mo <sub>10</sub> _copr	10MoO <sub>3</sub> /Ce <sub>0.70</sub> Zr <sub>0.30</sub> O <sub>2</sub>	Co-precipitation	90 °C

**Table 2.** Lattice parameters (*a*) for the impregnated samples, both determined by the XRD data and estimated (by using Vegard's law).

Sample	<i>a</i> (Calculated) [nm]	<i>a</i> (Vegard's Law) [nm]	Crystal Size [nm]
CeZr <sub>0</sub> Mo <sub>10</sub> _imp	0.54266	0.54113	11.1
CeZr <sub>15</sub> Mo <sub>10</sub> _imp	0.54080	0.53690	5.3
CeZr <sub>30</sub> Mo <sub>10</sub> _imp	0.53795	0.53266	7.8

Figure 2 reports the DTA-TG plot of sample CeZr<sub>0</sub>Mo<sub>10</sub>\_imp, confirming the hypothesis that the pure ceria support is already fully crystallized upon precipitation. In fact, such a thermograph reveals the presence of only two thermal events: the first one ( $\alpha$ ), endothermic, occurring at about 100 °C (paired with a weight loss of about 6%) and attributable to adsorbed water evolution, while the second one ( $\beta$ ), exothermic, occurring at  $\approx$ 620 °C (paired with a very small weight loss of <1%) and being very likely attributable to Mo oxide crystallization, as MoO<sub>3</sub> can exist in three different states: amorphous, monoclinic ( $\beta$ -hexagonal), or orthorhombic ( $\alpha$ -rectangular) [47]. However, given the adopted calcination treatment at 450 °C, the impregnated MoO<sub>3</sub> remains amorphous within all the prepared samples.

Table 2 reports the lattice parameter (*a*), both determined by the XRD data and estimated by using Vegard's law [48] of the three impregnated samples, along with their crystal size calculated by using the Williamson-Hall method.

The values of lattice parameters *a* for the impregnated samples are well aligned with each other and sufficiently aligned with the estimation given from Vegard's law (by using *a* = 0.54113 nm for pure CeO<sub>2</sub>, ICDD card n. 34-0394, and *a* = 0.51291 nm for pure ZrO<sub>2</sub>, ICDD card n. 81-1550), considering that the CeZr<sub>0</sub>Mo<sub>10</sub>\_imp sample has a higher cell parameter than the corresponding literature value. Furthermore, the inspection of the diffraction patterns in Figure 1 and the reported trend of the lattice parameter suggests the presence of a small amount of amorphous phase in the impregnated samples doped with Zr. The crystal size of the impregnated samples is pretty small, exhibiting no significant differences. As known, such a feature frequently promotes agglomeration phenomena leading to irregular powder morphology, as observed also in these samples (see Figure S1) [43].

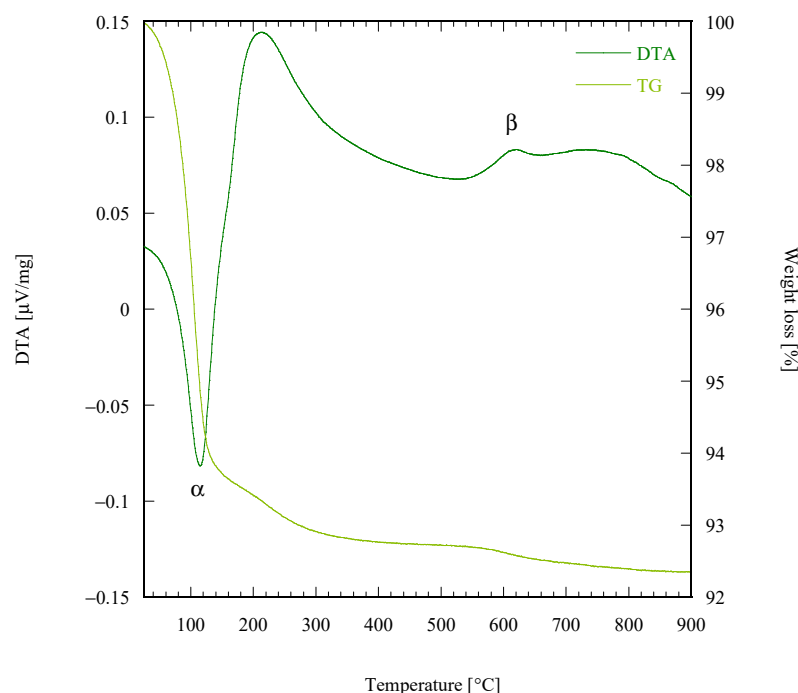


**Figure 2.** DTA/TG of sample CeZr<sub>0</sub>Mo<sub>10</sub>\_imp.

Figure 3 shows the diffraction patterns of all the co-precipitated catalysts (i.e., CeZr<sub>0</sub>Mo<sub>10</sub>\_copr, CeZr<sub>15</sub>Mo<sub>10</sub>\_copr, and CeZr<sub>30</sub>Mo<sub>10</sub>\_copr).

In general terms, all co-precipitated samples are found to be less crystalline compared to their corresponding impregnated samples, very likely because during co-precipitation in a single step (Ce-Zr-Mo) with NH<sub>3</sub> at high temperatures, the presence of Mo can hinder the crystallization of the samples, as already observed for similar systems [49].

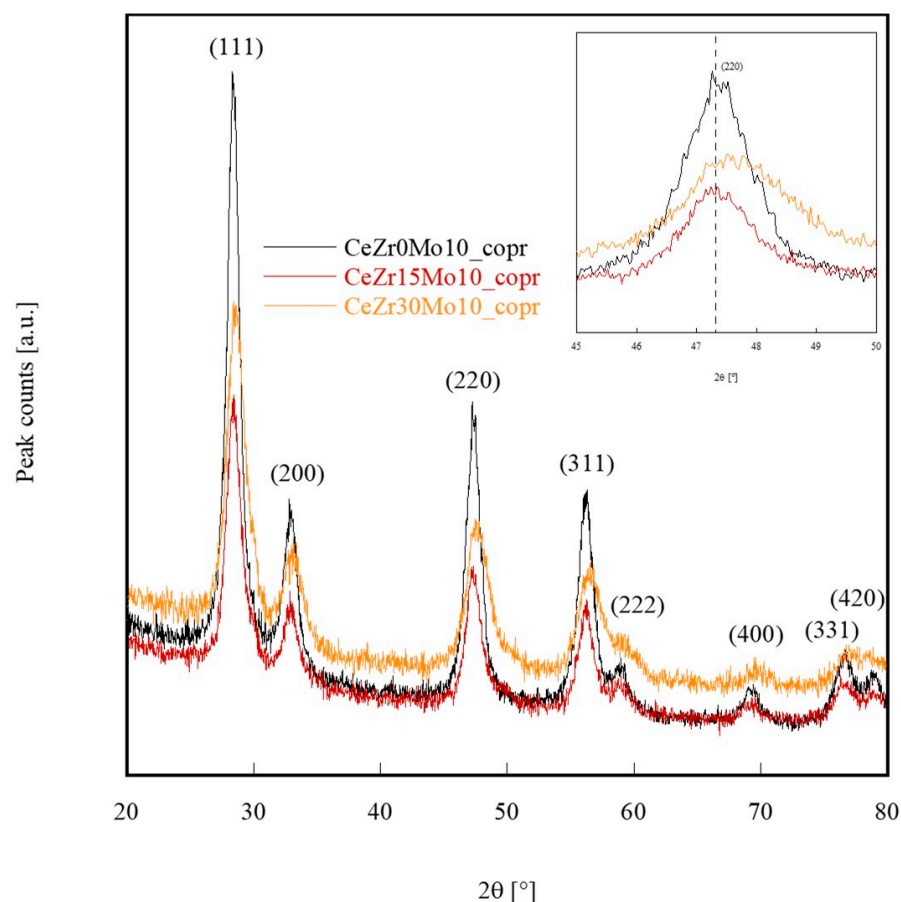
For the co-precipitated samples, a clear trend in the lattice parameter from their diffractograms is not discernible. Approximately, sample CeZr<sub>0</sub>Mo<sub>10</sub>\_copr (Zr = 0%) and CeZr<sub>15</sub>Mo<sub>10</sub>\_copr (Zr = 15%) share the same lattice parameter (as their peaks are virtually overlapped), while the lattice parameter of sample CeZr<sub>30</sub>Mo<sub>10</sub>\_copr (Zr = 30%) is found to be smaller (peaks shifted towards higher angles, as observable in the inset of Figure 3). Moreover, when comparing the diffractograms of sample CeZr<sub>15</sub>Mo<sub>10</sub>\_imp and sample CeZr<sub>15</sub>Mo<sub>10</sub>\_copr individually (both with a nominal Zr content of 15%), the lattice parameter of the impregnated sample appears to be slightly lower than that of its co-precipitated counterpart.

Table 3 reports the lattice parameter (*a*), both determined by the XRD data and estimated by using Vegard's law of the three co-precipitated samples, along with their crystal size calculated by using the Williamson-Hall method.

**Table 3.** Lattice parameters (*a*) for the co-precipitated samples, both determined by the XRD data and estimated (by using Vegard's law).

Sample	<i>a</i> (Calculated) [nm]	<i>a</i> (Vegard's Law) [nm]	Crystal Size [nm]
CeZr <sub>0</sub> Mo <sub>10</sub> _copr	0.54225	0.54113	9.5
CeZr <sub>15</sub> Mo <sub>10</sub> _copr	0.54227	0.53690	5.4
CeZr <sub>30</sub> Mo <sub>10</sub> _copr	0.54047	0.53266	4.0





**Figure 3.** XRD patterns of samples CeZr<sub>0</sub>Mo<sub>10</sub>\_copr, CeZr<sub>15</sub>Mo<sub>10</sub>\_copr, and CeZr<sub>30</sub>Mo<sub>10</sub>\_copr, calcined at 450 °C for 1 h. The inset highlights the detail of the (220) peak of CeZr<sub>0</sub>Mo<sub>10</sub>\_copr, CeZr<sub>15</sub>Mo<sub>10</sub>\_copr, and CeZr<sub>30</sub>Mo<sub>10</sub>\_copr diffraction patterns (dashed line indicates precise (220) peak position for sample CeZr<sub>0</sub>Mo<sub>10</sub>\_copr).

In the case of the co-precipitated samples, the de facto constancy of  $a$  between CeZr<sub>0</sub>Mo<sub>10</sub>\_copr and CeZr<sub>15</sub>Mo<sub>10</sub>\_copr suggests that there is no zirconia in the precipitated fluorite phase, even in the case of a nominal 15% of Zr, which obviously precipitated in an amorphous phase either composed by pure zirconia or by zirconium molybdates. Conversely, the decrease in  $a$  for sample CeZr<sub>30</sub>Mo<sub>10</sub>\_copr indicates that in this case Zr has entered the ceria fluorite-like structure. Finally, the nearly coincident values of  $a$  for the CeZr<sub>30</sub>Mo<sub>10</sub>\_copr sample and the CeZr<sub>15</sub>Mo<sub>10</sub>\_imp sample suggest that in the former sample approximately half of the nominal content of zirconium (30%) is amorphous and the rest is in a solid solution with CeO<sub>2</sub>. From these observations, it can be deduced that in the co-precipitation with ammonia in a single step, the simultaneous presence of soluble Mo salts and Zr cations in the aqueous environment (at about 100 °C) might lead to the formation of binary Mo-Zr compounds, for example, amorphous zirconium molybdates, which reduces available zirconium to be dissolved in the lattice of cerium oxide (CeO<sub>2</sub>) (this because, with the same nominal Zr content, the co-precipitated samples show higher lattice parameters compared to their corresponding impregnated samples, evidencing a quantity of Zr dissolved in the ceria lattice effectively less than the nominal one). Also, for the coprecipitated samples, the crystal size is very small and, not surprisingly, similar to the corresponding impregnated catalysts, due to the same synthesis method used to prepare the support. Therefore, also the coprecipitated catalysts exhibit agglomeration phenomena and non-uniform powder morphology (see Figure S2).

Figure 4 shows the N<sub>2</sub> absorption-desorption isotherms for all the prepared catalysts. It is clearly visible that samples prepared by co-precipitation and impregnation,

Figures 4a and 4b, respectively, display similar behavior when varying the Zr content. In particular, the shape of the isotherms can be described as type IV with a hysteresis loop classifiable as H2b. The latter, generated by the pore-blocking effect, is characterized by a non-steep evaporation branch due to a wide distribution of necks [50,51]. For both sets of samples, the zirconium-free catalyst shows an isotherm that clearly differs from the others concerning the condensation branch at  $p/p^0$  greater than 0.6. Despite a certain degree of overlap with the other adsorption curves, condensation is clearly delayed, indicating the presence of larger mesopores [52]. This interpretation is confirmed by the pore size distribution curves presented in Figure 5, *vide infra*. The assignment of the hysteresis loop in the case of the CeZr<sub>0</sub>Mo<sub>10</sub>\_copr and CeZr<sub>0</sub>Mo<sub>10</sub>\_imp samples is less straightforward. While it might also correspond to an H1-type, observed in samples where the width of the distribution of the necks is similar to that of the pores, it could also tentatively be assigned to an H3-type associated with a type II isotherm [53]. The latter situation, also referred to as pseudo-type II isotherm, is associated with metastability of the adsorbed multilayer (and delayed capillary condensation) and is due to the low degree of pore curvature and non-rigidity of the aggregate structure [54]. This second hypothesis seems less convincing due to the lack of the characteristic step-down to close the hysteresis [55].

When necks are below a certain critical size (5–6 nm for N<sub>2</sub> ads at 77 K), cavitation is the phenomenon that might govern the evaporation process (the molecules present in the cavity evaporate towards the surrounding bulk gas through a mass transfer mechanism through the pore neck), bringing the hysteresis closure point to a  $p/p^0$  value of about 0.4 [53,56].

In this situation, the pore size distribution is best achieved by the adsorption branch since the cavitation pressure is solely dependent on the thermophysical properties of the fluid present in the porous cavity. The pore size distribution, PSD, is shown in Figure 5. As expected from the adsorption/desorption isotherm analysis, all samples exhibit pore sizes within the mesopore range. It is possible to observe that overall, the samples prepared by impregnation, Figure 5b, exhibit smaller pore sizes than those prepared by coprecipitation, Figure 5a, with curves closing for smaller values of pore diameter. Furthermore, as expected from the isotherm analysis, the zirconium-free samples possess larger pore sizes, greater than 50 Å.

Table 4 shows the specific surface area and the total pore volume values obtained by processing the adsorption/desorption isotherms. In line with what is expected from the larger volumes of adsorbed nitrogen (the adsorption isotherms of co-precipitates close at higher values than those of impregnates), in Figure 5, the surface area values are higher for samples prepared by coprecipitation. Finally, the total pore volume gradually decreases with increasing zirconium.

**Table 4.** BET specific surface area,  $S_{\text{BET}}$ , and total pores volume,  $V_p$ , adsorbed NH<sub>3</sub> (calculated from NH<sub>3</sub>-TPD) and H<sub>2</sub> consumption (calculated from H<sub>2</sub>-TPR) of all prepared catalysts.

Sample	$S_{\text{bet}}$ (m <sup>2</sup> g <sup>−1</sup> ) <sup>a</sup>	$V_p$ (cm <sup>3</sup> g <sup>−1</sup> )	Adsorbed NH <sub>3</sub> (μmol g <sup>−1</sup> )	H <sub>2</sub> Uptake (μmol g <sup>−1</sup> )
CeZr <sub>0</sub> Mo <sub>10</sub> _copr	113	0.302	203	1133
CeZr <sub>15</sub> Mo <sub>10</sub> _copr	108	0.164	171	1351
CeZr <sub>30</sub> Mo <sub>10</sub> _copr	118	0.117	174	1402
CeZr <sub>0</sub> Mo <sub>10</sub> _imp	75	0.239	140	955
CeZr <sub>15</sub> Mo <sub>10</sub> _imp	116	0.116	194	1081
CeZr <sub>30</sub> Mo <sub>10</sub> _imp	92	0.090	144	1374

<sup>a</sup> relative pressure range of 0.18–0.28.



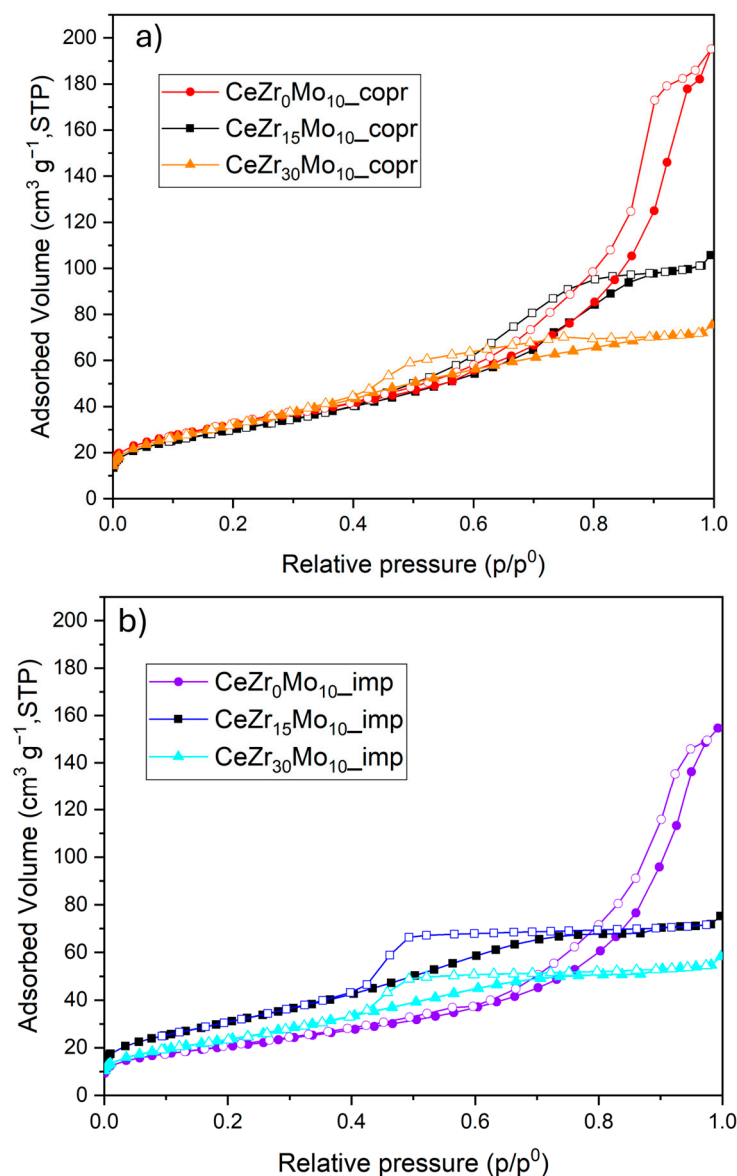


**Figure 4.** N<sub>2</sub> adsorption/desorption isotherms at 77 K of (a) samples CeZr<sub>0</sub>Mo<sub>10</sub>\_copr, CeZr<sub>15</sub>Mo<sub>10</sub>\_copr, and CeZr<sub>30</sub>Mo<sub>10</sub>\_copr, and (b) CeZr<sub>0</sub>Mo<sub>10</sub>\_imp, CeZr<sub>15</sub>Mo<sub>10</sub>\_imp, and CeZr<sub>30</sub>Mo<sub>10</sub>\_imp. Adsorption (solid markers) and desorption curves (empty markers).

The textural properties were complemented with redox and surface acidity properties to correlate the chemical, physical, and structural characteristics with the catalytic activity of the tested samples.

H<sub>2</sub>-TPR was performed to investigate the reducibility of the samples, indicating their ability to oxidize gaseous molecules. The H<sub>2</sub>-TPR curves, obtained in the 50–700 °C temperature range and not normalized for the mass of the samples, are presented in Figure 6a. They show a single peak with a maximum in the 520–570 °C temperature range, which can be attributed to the reduction of surface cerium species from Ce<sup>4+</sup> to Ce<sup>3+</sup> and the reduction of octahedral molybdenum groups, weakly bound to the surface with varying degrees of polymerization, Mo<sup>6+</sup> to Mo<sup>4+</sup> [57]. By accurate inspection of Figure 6a, it can be observed that both in the set of impregnated samples and in the set of coprecipitated ones, samples containing 30% Zr show a slightly higher peak temperature, whereas for the other samples in each set the difference in peak temperature is not significant. Thus, in our opinion, no relevant inference can be deduced by the peak temperatures in Figure 6a. On the contrary, a clear trend can be detected for the amount of consumed H<sub>2</sub> (see Table 4), inasmuch as it

increases with the increase of Zr content for both impregnated and coprecipitated samples. This finding confirms literature evidence reporting how the presence of Zr in the lattice of  $\text{CeO}_2$  favors the formation of oxygen vacancy [58], i.e., favors the reducibility of cerium; that also agrees with our XRD results showing the presence of Zr in the  $\text{CeO}_2$  lattice in substitutional position. Moreover, the co-precipitated catalysts show slightly higher  $\text{H}_2$  consumption values than the impregnated ones. Thus, the  $\text{CeZr}_0\text{Mo}_{10}\text{_{cpr}}$  sample has the lowest value, while the  $\text{CeZr}_{30}\text{Mo}_{10}\text{_{cpr}}$  sample has the highest value.

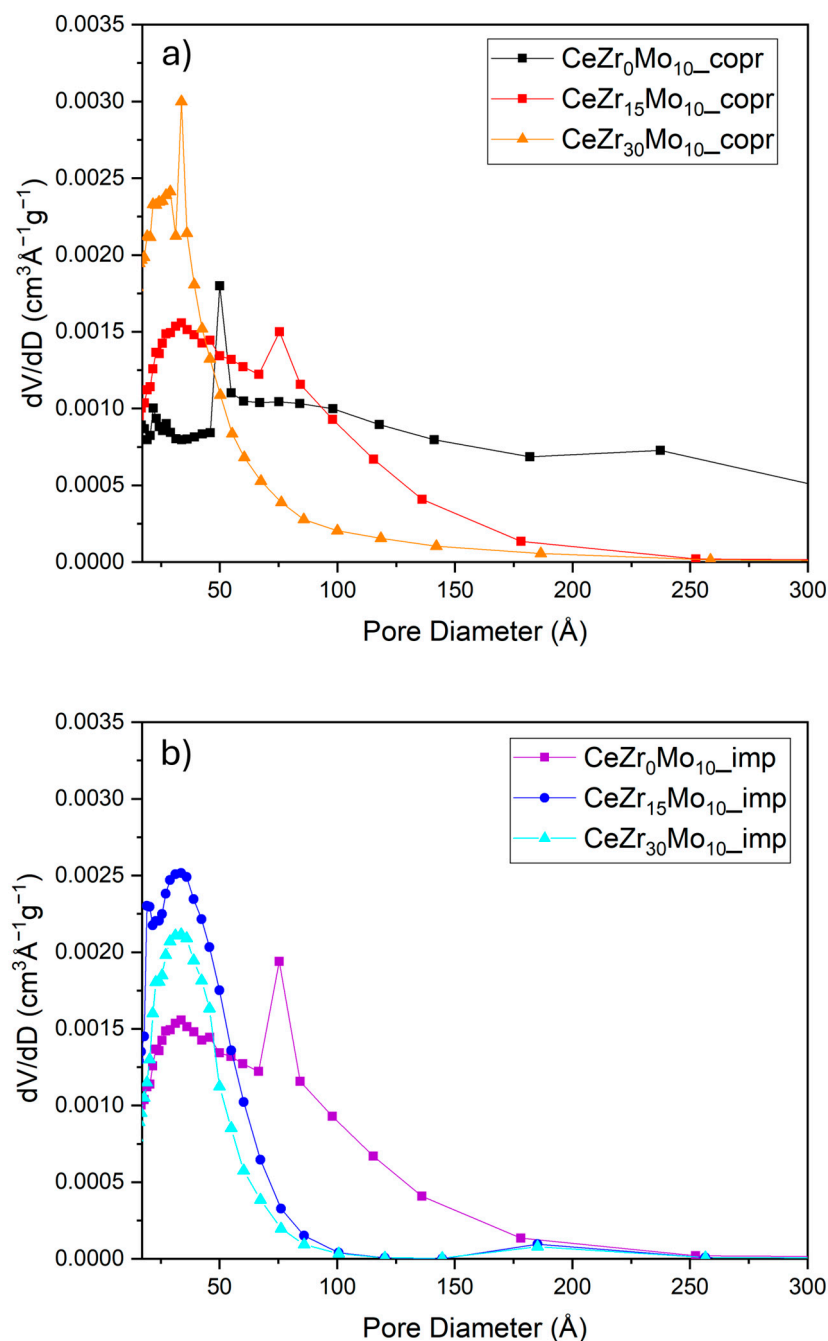


**Figure 5.** Pore size distribution of samples (a)  $\text{CeZr}_0\text{Mo}_{10}\text{_{cpr}}$ ,  $\text{CeZr}_{15}\text{Mo}_{10}\text{_{cpr}}$ , and  $\text{CeZr}_{30}\text{Mo}_{10}\text{_{cpr}}$  and (b)  $\text{CeZr}_0\text{Mo}_{10}\text{_{imp}}$ ,  $\text{CeZr}_{15}\text{Mo}_{10}\text{_{imp}}$ , and  $\text{CeZr}_{30}\text{Mo}_{10}\text{_{imp}}$ .

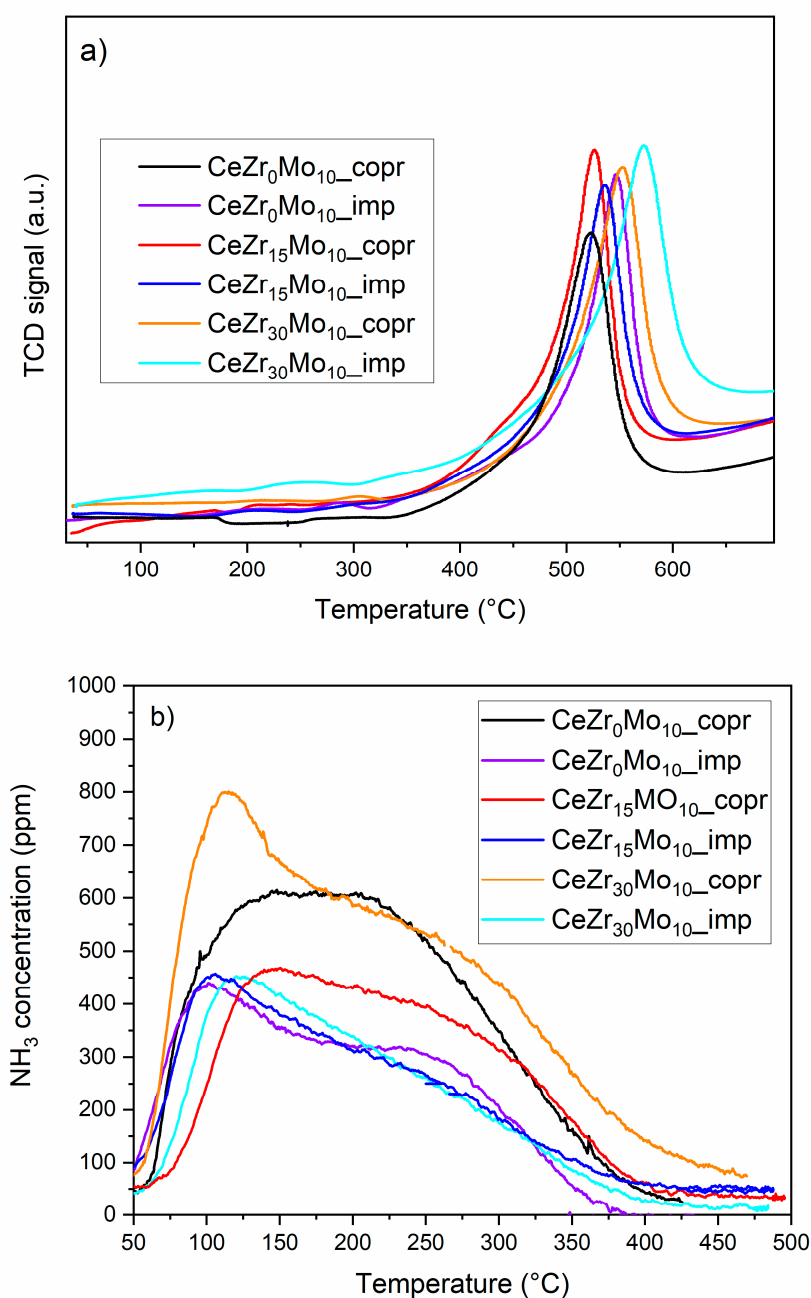


**Figure 6.**  $H_2$ -TPR curves (a) and  $NH_3$ -TPD curves (b) of the variously prepared samples.

$NH_3$ -TPD analysis was performed to study the presence and nature of the acid sites and the interaction of ammonia, i.e., the main reactant in  $NO_x$ -SCR, with the catalyst surface. The  $NH_3$ -TPD curves, not normalized for the mass of the samples, are reported in Figure 6b. All the tested catalysts show ammonia desorption in the 75–400  $^{\circ}C$  temperature range, corresponding to ammonia desorbed from acid sites of varying strength, generally categorized as weak, medium, and strong acid sites occurring in the 180–250  $^{\circ}C$ , 260–330  $^{\circ}C$ , and 340–500  $^{\circ}C$  temperature ranges, respectively [57]. The tested catalysts primarily exhibit weak and medium acid sites, with a similar trend across all samples, regardless of the adopted synthesis method or Zr addition. The values of adsorbed  $NH_3$ , reported in Table 4, do not show a clear dependence on these parameters too, except for a direct correlation between specific surface area and adsorbed  $NH_3$ .

Then, Figure 7 reports the catalytic activity of all the prepared catalysts (measured as the degree of conversion of  $NO_x$  fed to the reactor) as a function of temperature.

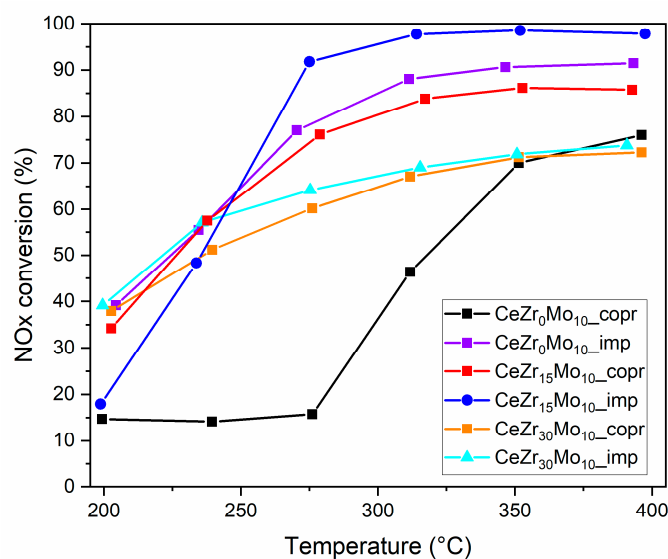


**Figure 7.** Catalytic activity (degree of NO<sub>x</sub> conversion fed to the catalytic reactor) of the variously prepared samples.

Generally speaking, the impregnated samples showed a better conversion than the co-precipitated ones, even though several marked differences between different samples can be observed. Particularly, it can be noted that the catalytic activities of the CeZr<sub>30</sub>Mo<sub>10</sub>\_imp and CeZr<sub>30</sub>Mo<sub>10</sub>\_copr catalysts were merely fair, achieving a maximum degree of NO<sub>x</sub> conversion of 70% at temperatures around 400 °C. Thus, no significant differences between the co-precipitated and impregnated catalysts containing 30 mol% of Zr were found. In this case, in fact, the obtained NO<sub>x</sub> conversion was lower than required for practical applications or reported in literature.

The sample CeZr<sub>0</sub>Mo<sub>10</sub>\_copr showed a constant NO<sub>x</sub> conversion degree of 15% up to about 280 °C. However, such counterintuitive behavior actually occurs at such low conversion values that it can essentially be ignored. With increasing temperature, CeZr<sub>0</sub>Mo<sub>10</sub>\_copr catalytic behavior significantly improved (reaching a conversion peak of about 75% near 390 °C), but even in this case, the NO<sub>x</sub> degree of conversion was lower than required for practical applications. The corresponding impregnated sample, i.e., CeZr<sub>0</sub>Mo<sub>10</sub>\_imp, exhibited the following behavior: at 200 °C, the conversion was about 40%, and with increasing temperature, the catalytic activity increased, reaching a conversion of 90% at about 350 °C and slightly exceeding 90% at about 390 °C. Therefore, in the case of undoped ceria support, a substantial difference emerged between the co-precipitated and impregnated samples, with the latter's catalytic activity proving to be very good and potentially useful for practical applications.

Finally, the CeZr<sub>15</sub>Mo<sub>10</sub>\_copr sample showed a conversion of about 35% at 200 °C, and with increasing temperature, the conversion substantially increased, reaching 85% at 350 °C. This conversion rate remained almost constant up to 390 °C. The impregnated counterpart, i.e., CeZr<sub>15</sub>Mo<sub>10</sub>\_imp, showed the best performance among all the tested samples; at 200 °C, the degree of NO<sub>x</sub> conversion was about 20%, and with increasing temperature, this conversion reached 70% at about 250 °C, surpassing 90% at about 280 °C, and from 290 °C up to 400 °C, it was practically equal to 100%.

N<sub>2</sub> selectivity was determined for all samples, and the corresponding results are shown in Figure 8. In a wide temperature range, N<sub>2</sub> selectivity of the catalysts is in general high, more than 80%. Moreover, the best samples in terms of NO<sub>x</sub> conversion achieved also selectivity close to 100%, confirming the best performance of CeZr<sub>15</sub>Mo<sub>10</sub>\_imp also from the viewpoint of selectivity.

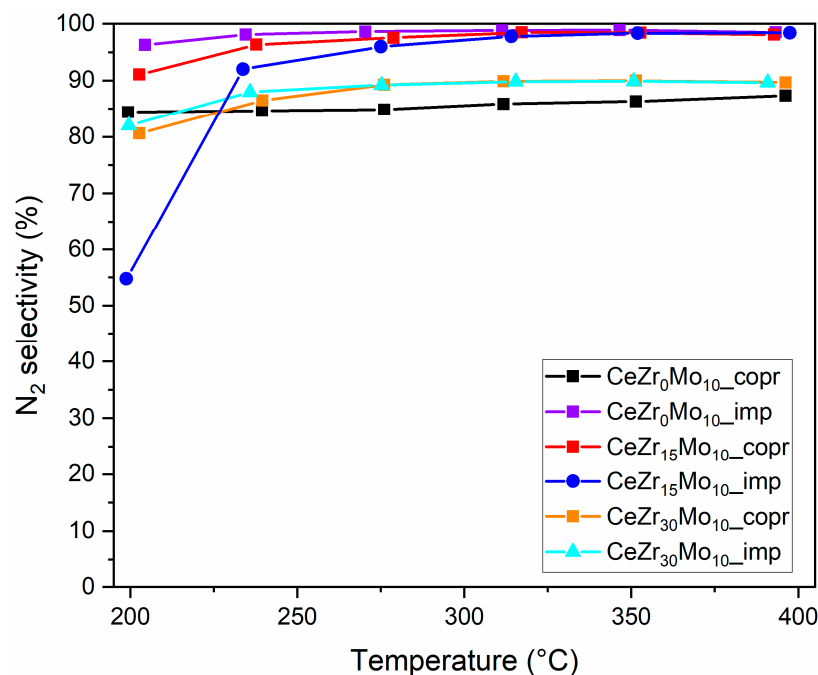


**Figure 8.** N<sub>2</sub> selectivity of the variously prepared samples.

Based on these results, the impregnation seems to be the most indicated synthesis method for Ce-Zr-Mo-based catalysts for the NH<sub>3</sub>-SCR reaction; in fact, despite the inferior textural and superficial properties (lower  $S_{\text{bet}}$ , lower amount of acid sites, lower redox ability), the impregnation method takes advantage of the full inclusion of Zr in the CeO<sub>2</sub> lattice upon support co-precipitation at room temperature and of avoiding potential side reactions occurring between Mo and Zr upon simultaneous Mo-Ce-Zr coprecipitation at 90 °C. Furthermore, a 15 mol% addition of Zr within the CeO<sub>2</sub> lattice seems to be the optimal doping for ceria-supported Mo-based catalysts, with the sample CeZr<sub>15</sub>Mo<sub>10</sub>\_imp that demonstrated to be the most performing NH<sub>3</sub>-SCR catalyst due to a high specific surface area, a high amount of weak and medium acid sites, and a moderate reducibility (i.e., sufficient to catalyze NO to NO<sub>2</sub> oxidation but not too high for oxidizing ammonia). Thus, CeZr<sub>15</sub>Mo<sub>10</sub>\_imp possesses all the necessary characteristics to be successfully employed in real technological applications.

### 3. Materials and Methods

Cerium (III) nitrate hexahydrate (Ce(NO<sub>3</sub>)<sub>3</sub>·6H<sub>2</sub>O, sourced from Carlo Erba, Cornaredo, MI, Italy), zirconium (IV) oxychloride octahydrate (ZrOCl<sub>2</sub>·8H<sub>2</sub>O), and ammonium heptamolybdate tetrahydrate ((NH<sub>4</sub>)<sub>6</sub>Mo<sub>7</sub>O<sub>24</sub>·4H<sub>2</sub>O) served as the starting materials for the catalysts. For the precipitation process, a 30% ammonia solution supplied by Carlo Erba, Italy, has been chosen, also based on previous authors results [59,60].

A typical synthesis of the different samples involved two distinct approaches: one where molybdenum was co-precipitated simultaneously with the ceria-zirconia supports, and another one where molybdenum was added onto a pre-formed ceria-zirconia support using a wet impregnation method (thus resulting in a two-step catalyst fabrication). In both procedures, the molybdenum content was consistently maintained at 10.0 wt% concerning the support mass.

All support materials own a nominal composition of Ce<sub>x</sub>Zr<sub>1-x</sub>O<sub>2</sub>, with x being either 1, 0.7, or 0.85, and were synthesized through a single-step co-precipitation process. The difference in the two series of co-precipitated samples was the choice of a different synthesis temperature, with simultaneous co-precipitation of ammonium heptamolybdate requiring T = 90 °C, while pure support co-precipitation occurs at room temperature.

Therefore, a typical synthesis involves the following steps:

- Cerium and zirconium precursors are dissolved in deionized water to achieve a total cation concentration of 0.1M; parallelly, a diluted ammonia solution (1M  $\text{NH}_3$ ) is prepared.
- Both solutions are stirred vigorously for 15 min to ensure complete dissolution and homogenization of the different precursors.
- An appropriate amount of the ammonia solution is gradually added to the cations-containing solution, either at room temperature in the case of sole support (doped/undoped ceria) or in a reflux setup at around 90 °C in the case of precursors containing molybdenum. This latter step is performed to ensure a significant excess of the base at a high temperature, leading to the formation of a Mo-containing powder precursor.
- After precipitation, the resulting suspensions are aged for a short period (several minutes), filtered, and thoroughly washed with deionized water and ethanol (to favor the complete elimination of Cl ions).
- Finally, all the co-precipitates are dried overnight at 80 °C and subsequently calcined at 450 °C for 1 h.

The supports precipitated at room temperature are subjected to a further impregnation step where the correct quantity of Mo is deposited onto the co-precipitated support. During this step, the support powder is “wet” with a concentrated ammonium heptamolybdate solution; subsequently, the obtained suspension was gradually heated with intensive stirring until all the water had evaporated. Finally, the obtained powders are dried overnight at 80 °C and subsequently calcined at 450 °C for 1 h.

The X-ray Diffraction (XRD) analysis of the powder samples was conducted using an X'Pert Philips diffractometer equipped with Cu K $\alpha$  radiation, covering a  $2\theta$  range of 20°–80° at a step width of 0.02° and a scanning time of 1 s per step. The patterns obtained from this analysis were matched with entries from the PDF-2 Release 2002 database for identification. The lattice parameters of the fluorite phase present in the samples were determined by using the Williamson-Hall method included in the software X'Pert HighScore 3.0 from Panalytical (Almelo, The Netherlands).

Thermal behavior of a selected sample was analyzed by simultaneous differential thermal analysis and thermogravimetric analysis (DTA-TG), using  $\alpha\text{-Al}_2\text{O}_3$  as a reference (Thermoanalyzer STA 409, Netzsch Instruments, Selb, Germany) and by using 10 °C min<sup>−1</sup> as the heating rate.

Nitrogen adsorption/desorption measurements were performed at −196 °C on a Quantachrome Autosorb 1C instrument, Boyton Beach, FL, USA, using around 100 mg of powder sample that had been previously outgassed at 250 °C for three hours to eliminate moisture and atmospheric impurities. The specific surface area of the samples was calculated based on the Brunauer-Emmett-Teller ( $S_{\text{BET}}$ ) method. The total pore volume  $V_{\text{p}}$  volume was determined at a relative pressure ( $p/p^0$ ) of 0.98, based on the desorption curve. Finally, the pore size distribution was derived by applying the Barrett-Joyner-Halenda (BJH) analysis to the desorption branch of the isotherms.

The  $\text{H}_2$ -TPR experiments were performed on the TPDRO 1100 instrument, Thermo Fisher Scientific, Waltham, MA, USA. Typically, 60 mg of the catalyst was placed in the reactor, pretreated in He stream to remove impurities at 250 °C. Following the pretreatment, the reactor was cooled down to 50 °C and reduced to 5%  $\text{H}_2/\text{Ar}$  20 mL/min flow with a 10 °C/min heating rate until 700 °C. The outlet gas was passed through a humidity trap and analyzed with a TCD detector that was previously calibrated with a CuO standard.

$\text{NH}_3$ -TPD were conducted in a quartz tube reactor placed in a PID-controlled vertical oven connected to an Infrared ABB Uras 26 analyser module (ABB S.p.A., Zurich, Switzerland) for ammonia quantification. A measured amount of catalyst powder was inserted in the reactor and degassed with 160 mL/min of  $\text{N}_2$  at 250 °C for 30 min, then the sample was cooled down to 100 °C and treated with 200 mL/min of 2000 ppm  $\text{NH}_3$  in a helium stream at constant temperature for 1 h. Subsequently, the physisorbed  $\text{NH}_3$  was removed by flowing 160 mL/min of  $\text{N}_2$  for 1 h. Finally, TPD was carried out by flowing 160 mL/min



of N<sub>2</sub>. The temperature was increased from 100 to 450 °C at a ramp rate of 5 °C/min and maintained at 450 °C for 30 min.

SCR catalytic tests on the experimental samples were conducted under the following conditions: 200 mg of each catalyst in a fixed bed with a gas flow of 600 mL/min composed of 10% O<sub>2</sub>, 2% H<sub>2</sub>O, 50 ppm NO, and NH<sub>3</sub> in N<sub>2</sub> as the carrier gas. This concentration was selected to mimic realistic conditions in low-emission scenarios and to ensure the accurate assessment of the catalytic activity under controlled, low-concentration conditions. The results presented were obtained after reaching a steady state (approximately 30 min waiting time) at the set temperature.

These catalytic tests were performed inside a quartz tubular reactor with an internal diameter of 10 mm. The catalyst powder was placed on a dense porous support within the reactor, which was then heated in a programmable vertical furnace. A thermocouple was used to monitor the reaction temperature, and specific analyzers (ABB AO2000 Uras and Limas, ABB S.p.A., Zurich, Switzerland) assessed the composition of the gaseous reaction products (NO, NO<sub>2</sub>, N<sub>2</sub>O, NH<sub>3</sub>, CO, and CO<sub>2</sub>). For each catalytic test, 200 mg of catalyst was used, with a gas flow rate of 600 mL/min, a catalyst mass/flow rate ratio of (0.02 g<sub>cat</sub>)/(mL s), and a gas hourly space velocity (GHSV) of 60,000 h<sup>-1</sup>.

#### 4. Conclusions

The challenge of NO<sub>x</sub> pollution still requires many research efforts to develop catalysts that are not only extremely efficient in reducing NO<sub>x</sub> emissions but also able to overcome the limitations of current technologies. To this regard, ceria-zirconia-supported molybdenum-based catalysts demonstrate impressive catalytic efficiency and robustness, even though their performance is markedly affected by the fabrication cycle and, particularly, by the choice of precipitating agent and Mo addition method. Thus, based on previous results obtained for similar systems, we intended to optimize the fabrication cycle of ceria-zirconia Mo-based catalysts for NH<sub>3</sub>-mediated NO<sub>x</sub> reduction.

Firstly, we compared the effects of different preparation methods, specifically wet impregnation versus co-precipitation. Impregnated catalysts exhibited superior catalytic performance compared to co-precipitated ones. This can be attributed to better dispersion and interaction of molybdenum with the support, as well as to the avoidance of side reactions between Mo and Zr upon co-precipitation. Secondly, we investigated the structural and surface properties, such as surface area and pore structure, of the differently prepared samples. Catalysts with higher surface areas and appropriate pore structures provided more active sites for the selective catalytic reduction reaction. The CeZr<sub>15</sub>Mo<sub>10</sub>\_imp catalyst maintained a high specific surface area with a balanced distribution of weak and medium acid sites, both important features for a NH<sub>3</sub>-SCR catalyst. Finally, H<sub>2</sub>-TPR analysis revealed that increased zirconium content enhances the reducibility of cerium, facilitating the conversion of NO<sub>x</sub>. The CeZr<sub>15</sub>Mo<sub>10</sub>\_imp catalyst exhibited moderate reducibility, which resulted optimal for promoting NO<sub>x</sub> reduction while preventing ammonia oxidation.

Thus, based on these considerations, we identified the optimal Zr doping for ceria-zirconia-supported Mo-based catalysts as 15 mol%, as the CeZr<sub>15</sub>Mo<sub>10</sub>\_imp showed a near 100% NO<sub>x</sub> conversion in a wide range of temperatures, i.e., a NO<sub>x</sub> conversion even higher than the most recent literature on NH<sub>3</sub>-mediated catalytic reduction (i.e., Mn/ZSM-5 reported by Pan et al. [61]), thus making it perfectly suitable for actual technological applications.

**Supplementary Materials:** The following supporting information can be downloaded at: <https://www.mdpi.com/article/10.3390/inorganics12080217/s1>, Figure S1: Exemplary SEM micrographs of sample CeZr<sub>15</sub>Mo<sub>10</sub>\_imp; Figure S2: Exemplary SEM micrographs of sample CeZr<sub>15</sub>Mo<sub>10</sub>\_cop.

**Author Contributions:** Conceptualization, G.D., L.S. and S.E.; methodology, L.S. and S.E.; investigation, L.S., V.M., N.B. and O.T.; resources, F.A.D. and G.D.; data curation, L.S., V.M., N.B. and O.T.; writing—original draft preparation, L.S. and O.T.; writing—review and editing, G.D., S.E. and F.A.D.; supervision, G.D. and F.A.D. All authors have read and agreed to the published version of the manuscript.

**Funding:** This research received no external funding.

**Data Availability Statement:** The raw data supporting the conclusions of this article will be made available by the authors on request due to privacy reasons.

**Conflicts of Interest:** The authors declare no conflicts of interest.

## References

- Kim, S.W.; Heckel, A.; McKeen, S.A.; Frost, G.J.; Hsie, E.Y.; Trainer, M.K.; Richter, A.; Burrows, J.P.; Peckham, S.E.; Grell, G.A. Satellite-observed US power plant NO<sub>x</sub> emission reductions and their impact on air quality. *Geophys. Res. Lett.* **2006**, *33*, L22812. [\[CrossRef\]](#)
- Wang, X.; Lei, Y.; Yan, L.; Liu, T.; Zhang, Q.; He, K. A unit-based emission inventory of SO<sub>2</sub>, NO<sub>x</sub> and PM for the Chinese iron and steel industry from 2010 to 2015. *Sci. Total Environ.* **2019**, *676*, 18–30. [\[CrossRef\]](#) [\[PubMed\]](#)
- Ashok, B. *NO<sub>x</sub> Emission Control Technologies in Stationary and Automotive Internal Combustion Engines: Approaches toward NO<sub>x</sub> Free Automobiles*; Elsevier: Amsterdam, The Netherlands, 2021.
- Zhang, S.; Zhao, P.; He, L.; Yang, Y.; Liu, B.; He, W.; Cheng, Y.; Liu, Y.; Liu, S.; Hu, Q.; et al. On-board monitoring (OBM) for heavy-duty vehicle emissions in China: Regulations, early-stage evaluation and policy recommendations. *Sci. Total Environ.* **2020**, *731*, 139045. [\[CrossRef\]](#) [\[PubMed\]](#)
- Shi, Z.; Peng, Q.; Jiaqiang, E.; Xie, B.; Wei, J.; Yin, R.; Fu, G. Mechanism, performance and modification methods for NH<sub>3</sub>-SCR catalysts: A review. *Fuel* **2023**, *331*, 125885. [\[CrossRef\]](#)
- Wu, T.; Guo, R.T.; Li, C.F.; You, Y.H.; Pan, W.G. Recent advances in core-shell structured catalysts for low-temperature NH<sub>3</sub>-SCR of NO<sub>x</sub>. *Chemosphere* **2023**, *333*, 138942. [\[CrossRef\]](#) [\[PubMed\]](#)
- Damma, D.; Ettireddy, P.R.; Reddy, B.M.; Smirniotis, P.G. A review of low temperature NH<sub>3</sub>-SCR for removal of NO<sub>x</sub>. *Catalysts* **2019**, *9*, 349. [\[CrossRef\]](#)
- Inomata, Y.; Hata, S.; Mino, M.; Kiyonaga, E.; Morita, K.; Hikino, K.; Yoshida, K.; Kubota, H.; Toyao, T.; Shimizu, K.-I.; et al. Bulk vanadium oxide versus conventional V<sub>2</sub>O<sub>5</sub>/TiO<sub>2</sub>: NH<sub>3</sub>-SCR catalysts working at a low temperature below 150 °C. *ACS Catal.* **2019**, *9*, 9327–9331. [\[CrossRef\]](#)
- Yan, Z.; Shan, W.; Shi, X.; He, G.; Lian, Z.; Yu, Y.; Shan, Y.; Liu, J.; He, H. The way to enhance the thermal stability of V<sub>2</sub>O<sub>5</sub>-based catalysts for NH<sub>3</sub>-SCR. *Catal. Today* **2020**, *355*, 408–414. [\[CrossRef\]](#)
- Lee, K.J.; Kumar, P.A.; Maqbool, M.S.; Rao, K.N.; Song, K.H.; Ha, H.P. Ceria added Sb-V<sub>2</sub>O<sub>5</sub>/TiO<sub>2</sub> catalysts for low temperature NH<sub>3</sub> SCR: Physico-chemical properties and catalytic activity. *Appl. Catal. B* **2013**, *142*, 705–717. [\[CrossRef\]](#)
- Zhao, S.; Peng, J.; Ge, R.; Yang, K.; Wu, S.; Qian, Y.; Xu, T.; Gao, J.; Chen, Y.; Sun, Z. Poisoning and regeneration of commercial V<sub>2</sub>O<sub>5</sub>-WO<sub>3</sub>/TiO<sub>2</sub> selective catalytic reduction (SCR) catalyst in coal-fired power plants. *Process Saf. Environ. Prot.* **2022**, *168*, 971–992. [\[CrossRef\]](#)
- Jeon, S.W.; Song, I.; Lee, H.; Kim, J.; Byun, Y.; Koh, D.J.; Kim, D.H. Enhanced SO<sub>2</sub> resistance of V<sub>2</sub>O<sub>5</sub>-WO<sub>3</sub>/TiO<sub>2</sub> catalyst physically mixed with alumina for the selective catalytic reduction of NO<sub>x</sub> with NH<sub>3</sub>. *Chem. Eng. J.* **2022**, *433*, 133836. [\[CrossRef\]](#)
- Zhu, H.; Song, L.; Li, K.; Wu, R.; Qiu, W.; He, H. Low-temperature SCR catalyst development and industrial applications in China. *Catalysts* **2022**, *12*, 341. [\[CrossRef\]](#)
- Consentino, L.; Pantaleo, G.; Parola, V.L.; Migliore, C.; Greca, E.L.; Liotta, L.F. NH<sub>3</sub>-NO SCR catalysts for engine exhaust gases abatement: Replacement of toxic V<sub>2</sub>O<sub>5</sub> with MnO<sub>x</sub> to improve the environmental sustainability. *Top. Catal.* **2023**, *66*, 850–859. [\[CrossRef\]](#)
- Reddy, B.M.; Ganesh, I.; Reddy, E.P. Study of dispersion and thermal stability of V<sub>2</sub>O<sub>5</sub>/TiO<sub>2</sub>–SiO<sub>2</sub> catalysts by XPS and other techniques. *J. Phys. Chem. B* **1997**, *101*, 1769–1774. [\[CrossRef\]](#)
- Zhang, Q.; Wu, Y.; Yuan, H. Recycling strategies of spent V<sub>2</sub>O<sub>5</sub>-WO<sub>3</sub>/TiO<sub>2</sub> catalyst: A review. *Resour. Conserv. Recycl.* **2020**, *161*, 104983. [\[CrossRef\]](#)
- Ding, L.; Wang, Y.; Qian, L.; Qi, P.; Xie, M.; Long, H. Flue gas deNO<sub>x</sub>ing spent V<sub>2</sub>O<sub>5</sub>-WO<sub>3</sub>/TiO<sub>2</sub> catalyst: A review of deactivation mechanisms and current disposal status. *Fuel* **2023**, *338*, 127268. [\[CrossRef\]](#)
- Zhang, Z.; Li, J.; Tian, J.; Zhong, Y.; Zou, Z.; Dong, R.; Gao, S.; Xu, W.; Tan, D. The effects of Mn-based catalysts on the selective catalytic reduction of NO<sub>x</sub> with NH<sub>3</sub> at low temperature: A review. *Fuel Process. Technol.* **2022**, *230*, 107213. [\[CrossRef\]](#)
- Mohan, S.; Dinesha, P.; Kumar, S. NO<sub>x</sub> reduction behaviour in copper zeolite catalysts for ammonia SCR systems: A review. *Chem. Eng. J.* **2020**, *384*, 123253. [\[CrossRef\]](#)
- Zhang, S.; Zhang, B.; Liu, B.; Sun, S. A review of Mn-containing oxide catalysts for low temperature selective catalytic reduction of NO<sub>x</sub> with NH<sub>3</sub>: Reaction mechanism and catalyst deactivation. *RCS Adv.* **2017**, *7*, 26226–26242. [\[CrossRef\]](#)
- Bonelli, B.; Tammaro, O.; Martinovic, F.; Nasi, R.; Dell’Agli, G.; Rivolo, P.; Giorgis, F.; Ditaranto, N.; Deorsola, F.A.; Esposito, S. Reverse Micelle Strategy for the Synthesis of MnO<sub>x</sub>-TiO<sub>2</sub> Active Catalysts for NH<sub>3</sub>-Selective Catalytic Reduction of NO<sub>x</sub> at Both Low Temperature and Low Mn Content. *ACS Omega* **2021**, *6*, 24562–24574. [\[CrossRef\]](#)
- Kumar, M.S.; Alphin, M.S.; Kumar, P.S.; Raja, S. A review on zeolite catalyst for de NO<sub>x</sub> performance in ammonia-selective catalytic reduction. *Fuel* **2023**, *334*, 126828. [\[CrossRef\]](#)
- Theis, J.R. The poisoning and desulfation characteristics of iron and copper SCR catalysts. *SAE Int. J. Fuels Lubr.* **2009**, *2*, 324–331. [\[CrossRef\]](#)

24. Wang, H.; Huang, B.; Yu, C.; Lu, M.; Huang, H.; Zhou, Y. Research progress, challenges and perspectives on the sulfur and water resistance of catalysts for low temperature selective catalytic reduction of NO<sub>x</sub> by NH<sub>3</sub>. *Appl. Catal. A Gen.* **2019**, *588*, 117207. [\[CrossRef\]](#)
25. Wang, Q.; Zhou, J.; Zhang, J.; Zhu, H.; Feng, Y.; Jin, J. Effect of ceria doping on the catalytic activity and SO<sub>2</sub> resistance of MnO<sub>x</sub>/TiO<sub>2</sub> catalysts for the selective catalytic reduction of NO with NH<sub>3</sub> at low temperatures. *Aerosol Air Qual. Res.* **2020**, *20*, 477–488. [\[CrossRef\]](#)
26. Wang, L.; Ren, Y.; Yu, X.; Peng, C.; Yu, D.; Zhong, C.; Hou, J.; Yin, C.; Fan, X.; Zhao, Z.; et al. Novel preparation method, catalytic performance and reaction mechanisms of Pr<sub>x</sub>Mn<sub>1-x</sub>O<sub>8</sub>/3DOM ZSM-5 catalysts for the simultaneous removal of soot and NO<sub>x</sub>. *J. Catal.* **2023**, *417*, 226–247. [\[CrossRef\]](#)
27. Mu, J.; Liu, J.; Qin, J.; Li, X.; Liu, B. Unveiling remarkable resistance to Pb poisoning over an Fe–Mo catalyst for low-temperature NH<sub>3</sub>-SCR: Poison transforms into a promoter. *Catal. Sci. Technol.* **2022**, *12*, 4388–4400. [\[CrossRef\]](#)
28. Mosrati, J.; Atia, H.; Eckelt, R.; Vuong, T.H.; Rabeah, J.; Mhamdi, M.; Armbruster, U. Ta and Mo oxides supported on CeO<sub>2</sub>-TiO<sub>2</sub> for the selective catalytic reduction of NO<sub>x</sub> with NH<sub>3</sub> at low temperature. *J. Catal.* **2021**, *394*, 325–339. [\[CrossRef\]](#)
29. Kwon, D.W.; Choi, J.; Nam, K.B.; Ha, H.P. New insight into the role of Mo–Sb addition towards VMoSbTi catalysts with enhanced activity for selective catalytic reduction with NH<sub>3</sub>. *Chem. Eng. J.* **2022**, *428*, 132078. [\[CrossRef\]](#)
30. Park, Y.J.; Kim, D.H.; Lee, J.H.; Ha, H.P.; Kwon, D.W. Unravelling the promotional effect of Nb and Mo on VO<sub>x</sub>-based catalysts for NO<sub>x</sub> reduction with NH<sub>3</sub>. *Appl. Surf. Sci.* **2023**, *614*, 156072. [\[CrossRef\]](#)
31. Yu, J.; Wang, C.; Wang, Y.; Qiu, L.; Yin, Y.; Li, X.; Zhao, F.; Chang, H. Poisoning Effects of HCl on MO<sub>x</sub>-WO<sub>3</sub>/TiO<sub>2</sub> (M= Mn, Ce and V) Catalysts for Selective Catalytic Reduction of NO<sub>x</sub> by NH<sub>3</sub>. *ChemCatChem* **2023**, *15*, e202201093. [\[CrossRef\]](#)
32. Liu, Y.; Deng, D.; Bao, X. Catalysis for selected C1 chemistry. *Chem* **2020**, *6*, 2497–2514. [\[CrossRef\]](#)
33. Iwasaki, M.; Dohmae, K.; Nagai, Y.; Sudo, E.; Tanaka, T. Experimental assessment of the bifunctional NH<sub>3</sub>-SCR pathway and the structural and acid-base properties of WO<sub>3</sub> dispersed on CeO<sub>2</sub> catalysts. *J. Catal.* **2018**, *359*, 55–67. [\[CrossRef\]](#)
34. Can, F.; Berland, S.; Royer, S.; Courtois, X.; Duprez, D. Composition-Dependent Performance of Ce<sub>x</sub>Zr<sub>1-x</sub>O<sub>2</sub> Mixed-Oxide-Supported WO<sub>3</sub> Catalysts for the NO<sub>x</sub> Storage Reduction–Selective Catalytic Reduction Coupled Process. *ACS Catal.* **2013**, *3*, 1120–1132. [\[CrossRef\]](#)
35. Zhao, L.; Zhang, Y.; Kang, M. Recent advances in heighten sulfur resistance of SCR catalysts: A review. *Environ. Eng. Res.* **2022**, *27*, 200642. [\[CrossRef\]](#)
36. Chao, Y.; Zhang, W.; Zhou, P.; Chen, H.; Lu, S.; Li, M.; Zhang, Q.; Gu, L.; Guo, S. An in-situ NH<sub>4</sub><sup>+</sup>-etched strategy for anchoring atomic Mo site on ZnIn<sub>2</sub>S<sub>4</sub> hierarchical nanotubes for superior hydrogen photocatalysis. *Sci. China Chem.* **2021**, *64*, 1716–1722. [\[CrossRef\]](#)
37. Du, P.; Hu, K.; Lyu, J.; Li, H.; Lin, X.; Xie, G.; Liu, X.; Ito, Y.; Qiu, H.-J. Anchoring Mo single atoms/clusters and N on edge-rich nanoporous holey graphene as bifunctional air electrode in Zn–air batteries. *Appl. Catal. B* **2020**, *276*, 119172. [\[CrossRef\]](#)
38. Zhang, F.; Liu, Z.; Chen, X.; Rui, N.; Betancourt, L.E.; Lin, L.; Xu, W.; Sun, C.-J.; Abeykoon, A.M.M.; Rodriguez, J.A.; et al. Effects of Zr doping into ceria for the dry reforming of methane over Ni/CeZrO<sub>2</sub> catalysts: In situ studies with XRD, XAFS, and AP-XPS. *ACS Catal.* **2020**, *10*, 3274–3284. [\[CrossRef\]](#)
39. Das, S.; Jangam, A.; Jayaprakash, S.; Xi, S.; Hidajat, K.; Tomishige, K.; Kawi, S. Role of lattice oxygen in methane activation on Ni-phyllsilicate@Ce<sub>1-x</sub>Zr<sub>x</sub>O<sub>2</sub> core-shell catalyst for methane dry reforming: Zr doping effect, mechanism, and kinetic study. *Appl. Catal. B* **2021**, *290*, 119998. [\[CrossRef\]](#)
40. Chen, J.; Carlson, B.D.; Toops, T.J.; Li, Z.; Lance, M.J.; Karakalos, S.G.; Choi, J.-S.; Kyriakidou, E.A. Methane Combustion Over Ni/Ce<sub>x</sub>Zr<sub>1-x</sub>O<sub>2</sub> Catalysts: Impact of Ceria/Zirconia Ratio. *ChemCatChem* **2020**, *12*, 5558–5568. [\[CrossRef\]](#)
41. Esposito, S.; Turco, M.; Bagnasco, G.; Cammarano, C.; Pernice, P. New insight into the preparation of copper/zirconia catalysts by sol–gel method. *Appl. Catal. A Gen.* **2011**, *403*, 128–135. [\[CrossRef\]](#)
42. Esposito, S.; Turco, M.; Bagnasco, G.; Cammarano, C.; Pernice, P.; Aronne, A. Highly dispersed sol–gel synthesized Cu–ZrO<sub>2</sub> materials as catalysts for oxidative steam reforming of methanol. *Appl. Catal. A Gen.* **2010**, *372*, 48–57. [\[CrossRef\]](#)
43. Spiridigliozzi, L.; Dell’Agli, G.; Biesuz, M.; Sglavo, V.M.; Pansini, M. Effect of the precipitating agent on the synthesis and sintering behavior of 20 mol % Sm-doped ceria. *Adv. Mater. Sci. Eng.* **2016**, *2016*, 6096123. [\[CrossRef\]](#)
44. Tammaro, O.; Paparo, R.; Chianese, M.; Ritacco, I.; Caporaso, L.; Camellone, M.F.; Esposito, S. Reverse micelle strategy for effective substitutional Fe-doping in small-sized CeO<sub>2</sub> nanocrystals: Assessment of adsorption and photodegradation efficiency of ibuprofen under visible light. *Chem. Eng. J.* **2024**, *479*, 147909. [\[CrossRef\]](#)
45. Dell’Agli, G.; Mascolo, G.; Mascolo, M.C.; Pagliuca, C. Drying effect on thermal behavior and structural modifications of hydrous zirconia gel. *J. Am. Ceram. Soc.* **2008**, *91*, 3375–3379. [\[CrossRef\]](#)
46. Shannon, R.D. Revised effective ionic radii and systematic studies of interatomic distances in halides and chalcogenides. *Acta Cryst.* **1976**, *A32*, 751–767. [\[CrossRef\]](#)
47. Wang, S.; Zhang, Y.; Ma, X.; Wang, W.; Li, X.; Zhang, Z.; Qian, Y. Hydrothermal route to single crystalline α-MoO<sub>3</sub> nanobelts and hierarchical structures. *Solid State Commun.* **2005**, *136*, 283–287. [\[CrossRef\]](#)
48. Vegard, L. Die Röntgenstrahlen im dienste der erforschung der materie. *Z. Für Krist.-Cryst. Mater.* **1928**, *67*, 239–259. [\[CrossRef\]](#)
49. Turco, R.; Bonelli, B.; Armandi, M.; Spiridigliozzi, L.; Dell’Agli, G.; Deorsola, F.A.; Esposito, S.; Di Serio, M. Active and stable ceria-zirconia supported molybdenum oxide catalysts for cyclooctene epoxidation: Effect of the preparation procedure. *Catal. Today* **2020**, *345*, 201–212. [\[CrossRef\]](#)

50. Thommes, M. Physical adsorption characterization of nanoporous materials. *Chem. Ing. Tech.* **2010**, *82*, 1059–1073. [[CrossRef](#)]
51. Cychosz, K.A.; Thommes, M. Progress in the physisorption characterization of nanoporous gas storage materials. *Engineering* **2018**, *4*, 559–566. [[CrossRef](#)]
52. Grosman, A.; Ortega, C. Capillary condensation in porous materials. Hysteresis and interaction mechanism without pore blocking/percolation process. *Langmuir* **2008**, *24*, 3977–3986. [[CrossRef](#)] [[PubMed](#)]
53. Thommes, M.; Kaneko, K.; Neimark, A.V.; Olivier, J.P.; Rodriguez-Reinoso, F.; Rouquerol, J.; Sing, K.S. Physisorption of gases, with special reference to the evaluation of surface area and pore size distribution (IUPAC Technical Report). *Pure Appl. Chem.* **2015**, *87*, 1051–1069. [[CrossRef](#)]
54. Sing, K.S.; Williams, R.T. Physisorption hysteresis loops and the characterization of nanoporous materials. *Adsorpt. Sci. Technol.* **2004**, *22*, 773–782. [[CrossRef](#)]
55. Manzoli, M.; Tammaro, O.; Marocco, A.; Bonelli, B.; Barrera, G.; Tiberto, P.; Allia, P.; Matéo-Vélez, J.-C.; Roggero, A.; Dantras, E.; et al. New insights in the production of simulated moon agglutinates: The use of natural zeolite-bearing rocks. *ACS Earth Space Chem.* **2021**, *5*, 1631–1646. [[CrossRef](#)]
56. Loi, Q.K.; Tan, S.J.; Do, D.D.; Nicholson, D. Lower closure point for nitrogen or argon adsorption in mesoporous solids: Window-induced evaporation or surface-induced cavitation? *Ind. Eng. Chem. Res.* **2021**, *60*, 15343–15351. [[CrossRef](#)]
57. Arfaoui, J.; Ghorbel, A.; Petitto, C.; Delahay, G. New MoO<sub>3</sub>-CeO<sub>2</sub>-ZrO<sub>2</sub> and WO<sub>3</sub>-CeO<sub>2</sub>-ZrO<sub>2</sub> nanostructured mesoporous aerogel catalysts for the NH<sub>3</sub>-SCR of NO from diesel engine exhaust. *J. Ind. Eng. Chem.* **2021**, *95*, 182–189. [[CrossRef](#)]
58. Yang, Z.; Wei, Y.; Fu, Z.; Lu, Z.; Hermansson, K. Facilitated vacancy formation at Zr-doped ceria (111) surfaces. *Surf. Sci.* **2008**, *602*, 1199–1206. [[CrossRef](#)]
59. Dell’Agli, G.; Mascolo, G. Agglomeration of 3 mol% Y-TZP powders synthesized by hydrothermal treatment. *J. Eur. Ceram. Soc.* **2001**, *21*, 29–35. [[CrossRef](#)]
60. Biesuz, M.; Spiridigliozzi, L.; Frasnelli, M.; Dell’Agli, G.; Sglavo, V.M. Rapid densification of Samarium-doped Ceria ceramic with nanometric grain size at 900–1100 °C. *Mater. Lett.* **2017**, *190*, 17–19. [[CrossRef](#)]
61. Pan, W.; He, J.; Huang, G.; Zhang, W.; Fang, D. Research Progress of the Selective Catalytic Reduction with NH<sub>3</sub> over ZSM-5 Zeolite Catalysts for NO<sub>x</sub> Removal. *Catalysts* **2023**, *13*, 1381. [[CrossRef](#)]

**Disclaimer/Publisher’s Note:** The statements, opinions and data contained in all publications are solely those of the individual author(s) and contributor(s) and not of MDPI and/or the editor(s). MDPI and/or the editor(s) disclaim responsibility for any injury to people or property resulting from any ideas, methods, instructions or products referred to in the content.